International Journal of Thermophysics, Vol. 25, No. 4, July 2004 (© 2004)

Bidirectional Reflection Measurements of Periodically Microstructured Silicon Surfaces[1]

Y. B. Chen,[2] Q. Z. Zhu,[2] T. L. Wright,[2] W. P. King,[2] and Z. M. Zhang[2,3]

Surface modifications have a great potential for selective emission and absorption for applications in photonics, energy conversion, and biosensing. Pattern-induced radiative property changes can be an important issue in the manufacturing and diagnostics of microelectronic devices. This work investigates the polarized diffraction of micromachined silicon wafers. Both one-dimensional (1-D) and two-dimensional (2-D) periodic microstructures are manufactured by plasma-assisted anisotropic etching. The rotating mask method is used to produce 2.25×10^6 2-D structures in a single sample ($7.5 \times 7.5\,\text{mm}^2$). Surface topography is characterized by using a scanning electron microscope (SEM). A bidirectional scatterometer with high accuracy and angular resolution measures the diffraction patterns from the microstructured silicon surfaces at a wavelength of 635 nm. The diffraction patterns follow the grating equation, which are caused by microstructures and their orientations. Predicted diffraction angles are in excellent agreement with the experimental results.

KEY WORDS: bidirectional reflection; diffraction; grating; scattering; silicon microstructures.

1. INTRODUCTION

The existence of micro/nanostructures can enhance the optical and radiative properties for photonic and energy conversion devices such as photodetectors, solar cells, thermophotovoltaic devices, optical filters and

[1]Paper presented at the Fifteenth Symposium on Thermophysical Properties, June 22–27, 2003, Boulder, Colorado, U.S.A.

[2]The George W. Woodruff School of Mechanical Engineering, Georgia Institute of Technology, Atlanta, Georgia 30332, U.S.A.

[3]To whom correspondence should be addressed. E-mail: zhuomin.zhang@me.gatech.edu

0195-928X/04/0700-1235/0 © 2004 Plenum Publishing Corporation

selective emitters [1–6]. In semiconductor processing, pattern-induced radiative property variations can be an important problem for the wafer temperature measurement and control [7,8]. An understanding of the diffraction profile may allow the etching depth and other features to be monitored during the microfabrication process [9]. Furthermore, surface waves can be excited with diffraction gratings, and sensors based on surface plasmon resonance can be used in biological and environmental detection [10,11]. Hence, it is imperative to investigate the directional and spectral radiative properties of microstructured surfaces.

Although it has been known for a long time that radiative properties can be modified by surface microstructures, earlier studies mainly dealt with rather simple geometries and were mostly for metallic surfaces [12]. The emergence of microfabrication has led to more systematic investigations of the influence of microstructure on radiative properties, especially thermal emission. Zhang et al. [13] provided a comprehensive review on the theoretical and experimental studies of radiative properties of semiconductor materials, including thin films and multilayer systems, rough surfaces, and periodical structures. Hesketh et al. [14,15] and Wang and Zemel [16] published a series of studies on the thermal emission from micromachined silicon surfaces and observed emissivity enhancement of deep and shallow grooves with a period between 10 and 22 μm. Recently, Greffet et al. [17] showed coherent infrared emission using a SiC grating with a period of 6.25 μm and a depth of 0.28 μm. The emission was enhanced in certain directions for a given wavelength or in a certain spectral region for a given direction. The origin of coherent thermal emission was attributed to the excitation of surface-phonon polaritons by the grating [17,18]. Sai et al. [19] fabricated two-dimensional (2-D) arrays of $2 \times 2\,\mu m^2$ reverse-pyramid microcavities on a silicon surface using wet etching and by then coating it with a metallic layer. Maruyama et al. [20] fabricated 2-D square-shaped microcavity arrays using dry etching with inductively coupled plasma (ICP). Coherent emission and reflection were observed in the near-infrared spectral region for the normal direction [19,20]. Cohn et al. [21] compared theoretical and experimental results of reflection from 1-D microcontoured metallic surfaces with sinusoidal, triangular, and rectangular profiles. Tang and Buckius [22] measured the bidirectional reflection from several 2-D microcontoured metallic surfaces and showed that the 1-D model is insufficient for 2-D structures.

Despite the large number of studies on the emission and reflection of microstructured surfaces, high-angular-resolution bidirectional reflection measurements of periodical structures rarely exist in the literature, especially for 2-D gratings. In the present study, we report the bidirectional reflection measurements for 1-D and 2-D microstructured silicon samples,

using a newly developed three-axis automated scatterometer (TAAS) [23]. The measured diffraction angles are compared with theoretical predictions. The experimental data may be useful for the validation of 2-D models based on rigorous electromagnetic wave theory. An understanding of the bidirectional reflection of microstructured surfaces may help future design of engineering surfaces with desired radiative properties.

2. SILICON MICROFABRICATION

The present study uses chemical vapor deposition, plasma etching, and other microfabrication techniques to create 1-D and 2-D microstructures. The initial designs are shown in Fig. 1, where P is the period, G is the width of the groove, and H is the height (depth). The actual structures may vary due to the process. A single photomask is used to generate both the 1-D and 2-D surface patterns. The photomask contains approximately 3000 squares, with two types of periodic line structures (patterns). The distance between the centers of adjacent lines is $5\,\mu$m ($P = 5\,\mu$m) for both structures. Pattern A has a linewidth of $1\,\mu$m, and pattern B has a linewidth of $4\,\mu$m. By exposing the wafer once with this photomask, a 1-D groove structures with a period of $5\,\mu$m and groove widths (G) of $4\,\mu$m (type A) and $1\,\mu$m (type B) can be fabricated using the standard photolithographic steps.

The 2-D fabrication is performed with a unique "double exposure method," in which the wafer being patterned is exposed once with the photomask in place and another time after the mask is rotated by 90°. Rotation of the mask allows for the fabrication of three different 2-D microstructures: pattern AA has $G_1 = G_2 = 4\,\mu$m, pattern BB has $G_1 = G_2 = 1\,\mu$m, and pattern AB has $G_1 = 1\,\mu$m and $G_2 = 4\,\mu$m. The grating period is the same in both directions, i.e., $P_1 = P_2 = 5\,\mu$m. The final product contains 2.25×10^6 structures in a single square sample ($7.5 \times 7.5\,\mathrm{mm}^2$). Heinzel et al. [5] used a similar method to obtain crossed gratings by rotating the wafer 90° between exposures.

The steps used in the 1-D and 2-D microstructure fabrication process are described as follows. First, the single crystal silicon (100) wafer is cleaned with organic solutions, rinsed with de-ionized water, and then dried with nitrogen gas. A layer of SiO_2, which will eventually serve as an etching mask for silicon, is deposited with plasma-enhanced chemical vapor deposition (PECVD) to a thickness of approximately $0.7\,\mu$m. Second, a positive photoresist is spun on top of the SiO_2 layer. Ultraviolet (UV) light is then exposed through the photomask, once to make the 1-D gratings and twice (by rotating the mask 90° between exposures) to create the 2-D structures. The photoresist that was exposed to the UV

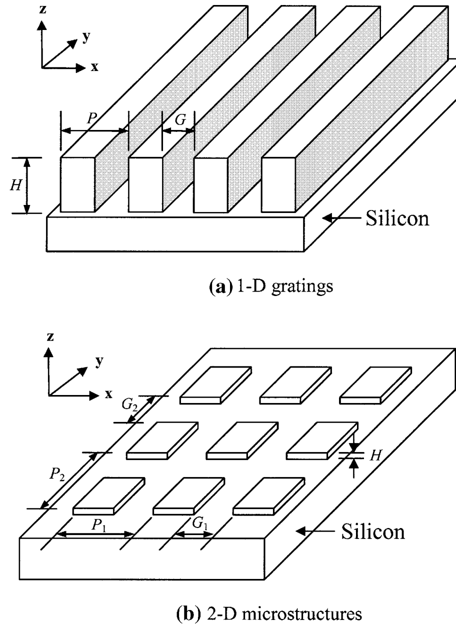

Fig. 1. Schematic of (a) 1-D gratings and (b) 2-D structured surfaces, where P is the grating period, G is the groove width, and H is the structure height (groove depth).

light is then removed, leaving the desired patterns on top of the SiO_2 layer. The unmasked SiO_2 is anisotropically etched away by reactive iron etching (RIE). Afterwards, the remaining photoresist is removed by acetone. At this point, the desired patterns are contained in the SiO_2 layer. Third, a Teflon layer is deposited and an ICP is used to anisotropically etch the silicon using a deep reactive ion etching (DRIE) technique, known as the Bosch process [24]. Deep etching of the silicon can be achieved by repeating the ICP etching process cycle. Finally, the remaining Teflon layer is burned away using oxygen plasma in the RIE, and the remaining SiO_2 is removed using buffered oxide etchant (BOE). The depth of the grooves depends on the number of Bosch process cycles completed and etching time used in each cycle.

A SEM is used to study the morphology of the fabricated structures, as shown in Fig. 2. In Fig. 2a, typical 1-D features (type A, $G = 4\,\mu$m) and their cross-sectional view are shown. It can be seen that the shape and dimension of the structures are uniformly produced with a period of $5\,\mu$m as expected. The shape is triangular because of the residual non-uniform and thin photoresist. This changes the pattern of the SiO_2 layer

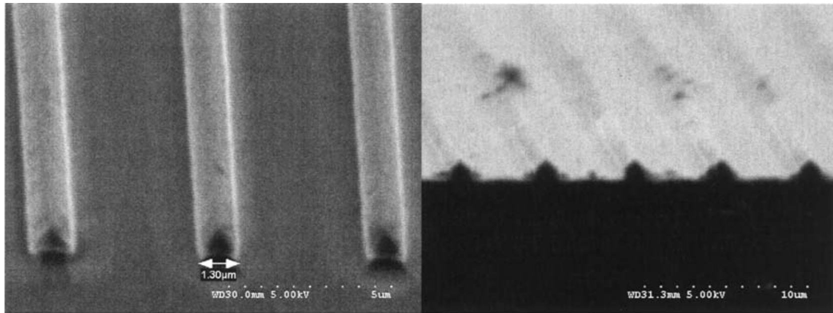

(a) 1-D (type A, $G = 4$ µm) features and their cross-sectional view

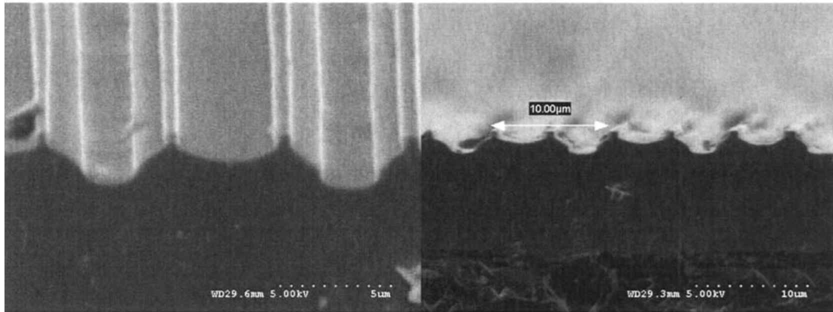

(b) 1-D (type B, $G = 1$ µm) features and their cross-sectional view

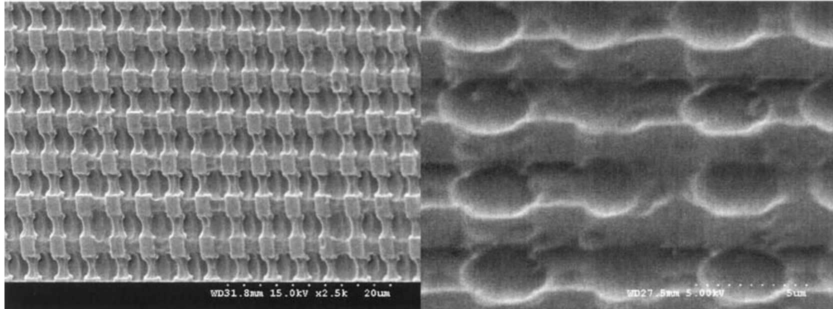

(c) 2-D (type AA, $G_1 = G_2 = 1$ µm) features and the magnification view

Fig. 2. Images obtained from SEM of three different samples. (a) 1-D features ($G = 4\,\mu$m) and their cross-sectional view; (b) 1-D features ($G = 1\,\mu$m) and their cross-sectional view; (c) 2-D features ($G_1 = G_2 = 1\,\mu$m) and their cross-sectional view.

so that the thickness is the largest at the center and decreases towards the edge during the RIE process. This SiO_2 pattern results in the triangular shape feature on the Si surface. The width at the feature bottom is approximately $1.3\,\mu$m, slightly more than expected, and the height is approximately $0.9\,\mu$m. Figure 2b shows the other type of 1-D feature (type

B, $G = 1\,\mu$m) and its cross-sectional view. The sample contains alternatively different depth valleys whose depths are 2.1 μm (deep) and 1.1 μm (shallow). These valleys are due to defects in the photomask and short exposure and development times. These valleys have a period of 5 μm, and the valleys of similar depth have a period which is 10 μm and are aligned. Furthermore, the cross-sectional view shows that the surface is not smooth but wavy, except for one groove shaped feature on the peak of each wave.

It can be seen from Fig. 2 that the fabricated structures are not the same as the initial design. These differences result from the balancing of the exposing and developing time for both patterns A and B. Features with a smaller linewidth (pattern A) need less exposure and development time than features with a larger linewidth (pattern B) to decrease the nonuniformity caused by the UV light diffraction and photoresist washing. Also, pattern B needs more time for the UV light and the developing chemicals to react with the bottom photoresist with the smaller opening (1 μm) on the photomask. Because the two patterns are on the same wafer for whole fabrication process, a balanced time is selected. As a result, the photoresist of pattern A is overexposed and overdeveloped so that uniform photoresist with smaller linewidth and height is remaining. Conversely, the photoresist of pattern B is underexposed and underdeveloped so that thicker photoresist is remaining, even some bottom photoresist under the UV light. The photoresist has continuous connection resulting in the wave shape and not the groove shape after removing the exposed parts.

Figure 2c shows the 2-D features and their magnification view (pattern BB, $G_1 = G_2 = 1\,\mu$m). It is clearly shown that each feature has almost a square top surface ($2.5 \times 2.5\,\mu m^2$) and is uniformly fabricated. The reduced top surface size might be caused by the overexposure in the lithographic step. The connections among the neighboring squares are caused by the remaining photoresist in the plasma etching process. The silicon surface at the bottom of the structures is not flat because of ditching and trenching, which occur when the side walls of the SiO_2 are not perfectly vertical. During the RIE process, some etchant ions will collide at a glancing angle with the inclined side walls before arriving at the silicon surface [24]. This gives a local increase in the etching rate, which leads to an unsmooth bottom surface.

3. BIDIRECTIONAL REFLECTION MEASUREMENTS

The bidirectional reflection of the 1-D and 2-D samples is measured using the TAAS, which includes a light source, a goniometric table, and a detection and data acquisition system [23]. The light source is a fiber-coupled diode laser at a wavelength of 635 nm. This wavelength is

widely used in laser light source and silicon is opaque at this wavelength. Different wavelength light sources will be studied in the future. The laser diode is mounted on a thermoelectrically cooled platform, which is maintained at a constant temperature. A current driver controls the power of the diode laser. This laser system has been shown to have excellent wavelength stability and power stability (0.2% over 24 h). The fiber output is 1–2 mW. The linear polarizer after the laser allows the selection of different polarizations. Since the sample is vertically mounted, the vertical polarization corresponds to the transverse electric (TE) wave while the horizontal polarization corresponds to the transverse magnetic (TM) wave. A beam splitter separates the light into two rays: one is incident on the sample being measured and the other is incident on a reference detector. The ratio of outputs from the two photodetectors is divided by the calibrated beam splitter ratio to obtain the *power ratio* η, which is the ratio of the reflected power to the incident power (i.e., $\eta = P_{\mathrm{r}}/P_{\mathrm{i}}$). The incident beam is collimated with a diameter of approximately 4 mm. The diameter of the precision aperture in front of the movable detector is 8 mm, large enough to collect the diffracted radiation at a given diffraction order, except when $\theta_{\mathrm{r}} > 60^{\circ}$. Furthermore, the small collecting solid angle (with a half-cone angle of 0.45°) yields a high angular resolution. The output of each photodiode is amplified by a trans-impedance amplifier and feeds into an input port of the lock-in amplifier. The lock-in amplifier sends an oscillating signal to the laser current controller, so that the output of the laser is modulated at the same frequency as that of the oscillating signal, resulting in a high signal-to-noise ratio. Since there are a number of samples on the same wafer, an $x-y$ translation stage is mounted on the sample holder to manually scan the wafer for measuring different samples.

A schematic drawing of the goniometric table is shown in Fig. 3a. Stages 1–3 are three high-accuracy step-motor controlled rotary stages. Stages 1 and 3 are coaxial, but their rotations are independently controlled. The intersection (O) of the axis of stages 1 and 2 is the center point of the goniometric table. The light source is fixed, and the incidence angle (θ_{i}) is varied by rotating stage 1, since $\theta_{\mathrm{i}} = \alpha$. A dial rotator is mounted on the sample holder to manually change the azimuthal angle (φ_i). Stages 2 and 3 are used to move the detector around point O. When β is changed from 0° to 90°, the detector arm moves up from the horizontal to the vertical positions. Here, γ can be varied from -180° to 180°. When $\gamma = 0^{\circ}$ and $\beta = 0^{\circ}$, the detector is between the laser and the sample and it blocks the beam. Figure 3b shows the incidence and reflection directions and the coordinate systems. The center point of the sample (point O) is the intersection of the x and y-axes, while the z-direction is normal to the sample. The y-axis is in the vertical direction,

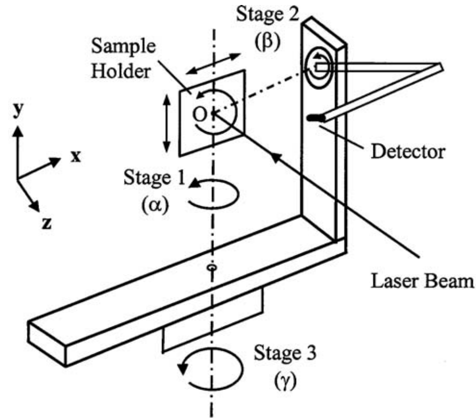

(a) Goniometric table

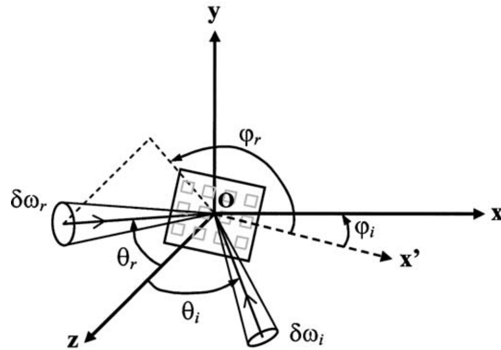

(b) Coordinate systems

Fig. 3. Schematic drawings of (a) the goniometric table and (b) the sample coordinate system. Three automatically controlled stages 1–3 rotate the sample (α), to change the incidence angle, and detector (β and γ), to change the reflection direction (θ_r, φ_r). A dial rotator mounted on the sample holder rotates the sample manually to change φ_i. An x–y stage moves the wafer so that different samples on the wafer can be scanned manually.

and the incident beam lies in the $x-z$ plane. The azimuthal angle φ_i with respect to the sample axis (x') can be changed by rotating the sample around the z-axis. The reflection direction θ_r and φ_r are determined by the position angles of the detector (β and γ), as well as the sample rotation. The following relations describe the coordinate transformation

between the reflection direction and the angular positions of stages:

$$\cos\theta_{\mathrm{r}} = \cos(\gamma - \alpha)\cos\beta,$$
$$\cos(\varphi_{\mathrm{r}} - \varphi_{\mathrm{i}}) = \frac{\sin(\gamma - \alpha)\cos\beta}{\sin\theta_{\mathrm{r}}}. \quad (1)$$

The bidirectional reflection measurement for a 1-D microstructured sample is performed when both the incident beam and reflected beam are perpendicular to the grooves on the sample. Consequently, $\beta = 0°$, $\varphi_{\mathrm{i}} = 0°$, and $\varphi_{\mathrm{r}} = 0°$ when $\gamma - \alpha < 0°$ and 180° when $\gamma - \alpha > 0°$. Only rotary stages 1 and 3 are used and the incidence and reflection angles are determined by $\theta_{\mathrm{i}} = \alpha$ and $\theta_{\mathrm{r}} = |\gamma - \alpha|$, respectively. The orientation of the sample is adjusted by rotating the dial rotator until all the reflected light spots lie in the horizontal plane of the experimental setup. Diffraction causes the reflection to exhibit discrete peaks according to the diffraction order $m(= 0, \pm 1, \pm 2, \ldots)$. The angle corresponding to the mth order of diffraction is determined by the well-known grating equation [25],

$$\sin\theta_{\mathrm{d}}^{(m)} = \sin\theta_{\mathrm{i}} + \frac{m\lambda}{\Lambda}, \quad (2)$$

where λ is the wavelength of the light source and Λ is the period of the structure ($\Lambda = P$ for 1-D gratings). Since the reflected power is confined to a very narrow angular range for each diffraction order, the detector only scans within $\pm 1.4°$ about each diffraction peak. The detector scans every 0.2° between $\pm 0.4°$ of the theoretical value and 0.5° from $-1.4°$ to $-0.4°$ and from 0.4° to 1.4°. This allows the measurement to be performed with a high angular resolution and within a reasonable amount of time.

For the 2-D microstructured surfaces, the diffraction can be measured similarly by varying the azimuthal angle φ_{i} (i.e., rotating the sample holder). For example, when $\varphi_{\mathrm{i}} = 0°$, two sides of the sample are parallel to the x- and y-axes; when $\varphi_{\mathrm{i}} = 45°$, the sample holder is rotated by 45° and the projection of the incident beam to the $x - y$ plane is parallel to the diagonal of the sample. Only α and γ need to be changed to vary the angle of incidence and to locate the diffraction peaks along the direction determined by φ_{i}.

To measure the hemispherical diffraction distribution, β needs to be changed as well. In this case, the detector is manually positioned to each diffraction peak, which is found by observation. The detector tube is covered by a cap with a cross mark at its center. The angles β and γ are changed by manually inputting their values to their controllers. When the reflected spot falls to the middle of the cross mark, the cap is removed and measurements are taken.

4. RESULTS AND DISCUSSION

Figure 4 shows the measurement results for a 1-D microstructured sample, corresponding to Fig. 2a with $G = 4\,\mu$m. The angles associated with the diffraction peaks are very close to the theoretical values calculated from Eq. (2) with a grating period $P = 5\,\mu$m. Within $\pm 2°$ of the retroreflection angle, the detector blocks the incidence beam, and the reflected power cannot be measured. These angles are marked by an "$\times$" sign in the figure. The diffraction patterns for normal incidence ($\theta_\mathrm{i} = 0°$) are almost symmetric with respect to the specular direction ($\theta_\mathrm{r} = 0°$). The power ratio does not always decrease as the absolute value of m increases. For example, the power ratios at $m = \pm 2$ are larger than those at $m = \pm 1$. The power ratio is generally larger for the TE wave than for the TM wave, except when $m = \pm 1$.

At $\theta_\mathrm{i} = 15°$ and $30°$, the zeroth-order diffraction is in the specular direction, where η is the largest. When θ_i increases from 15° to 30°, the power ratio at $m = 0$ increases for a TE wave but decreases for a TM wave. This trend is the same as the reflectance of a smooth dielectric surface, which can be predicted by the Fresnel equations. However, the power ratio is not symmetric with respect to the specular direction, which can not be explained by the equations. For example, the power ratio for $m = -2$ is much larger than that for $m = 2$ in Fig. 4b and c. Furthermore, at $\theta_\mathrm{i} = 30°$, η is larger for the TE wave at $m = -2$ but smaller for the TM wave at $m = 2$. In addition, significant reflection is observed for the highest orders ($m = -10$ and -11) at $\theta_\mathrm{i} = 30°$.

The measurement results for another 1-D microstructured sample ($G = 1\,\mu$m, corresponding to Fig. 2b) are plotted in Fig. 5. While the angles of the diffraction peaks are very close to the theoretical values, the power ratio is not symmetric with respect to the specular direction at $\theta_\mathrm{i} = 0°$. For the TM wave, η is largest at $m = -1$; however, for the TE wave, η is largest at $m = -7$. This suggests that the structure on the sample is not symmetric. The power ratio is distributed more evenly for all orders of diffraction. Furthermore, some small peaks were observed between the peaks corresponding to a grating period of $5\,\mu$m. Their locations are identified by the triangular indicators underneath the curves in Fig. 5. These peaks correspond to the microstructures with the $10\,\mu$m period. It can be seen from the SEM image of the features cross-sectional view (Fig. 2b) that there exist deep and shallow groove pairs with a period of $10\,\mu$m. The photomask was inspected under an optical microscope, and some defects in the lines for this structure were found. These results suggest that bidirectional reflection measurements are sensitive to the micro-structural defects and could therefore be used as a diagnostic tool.

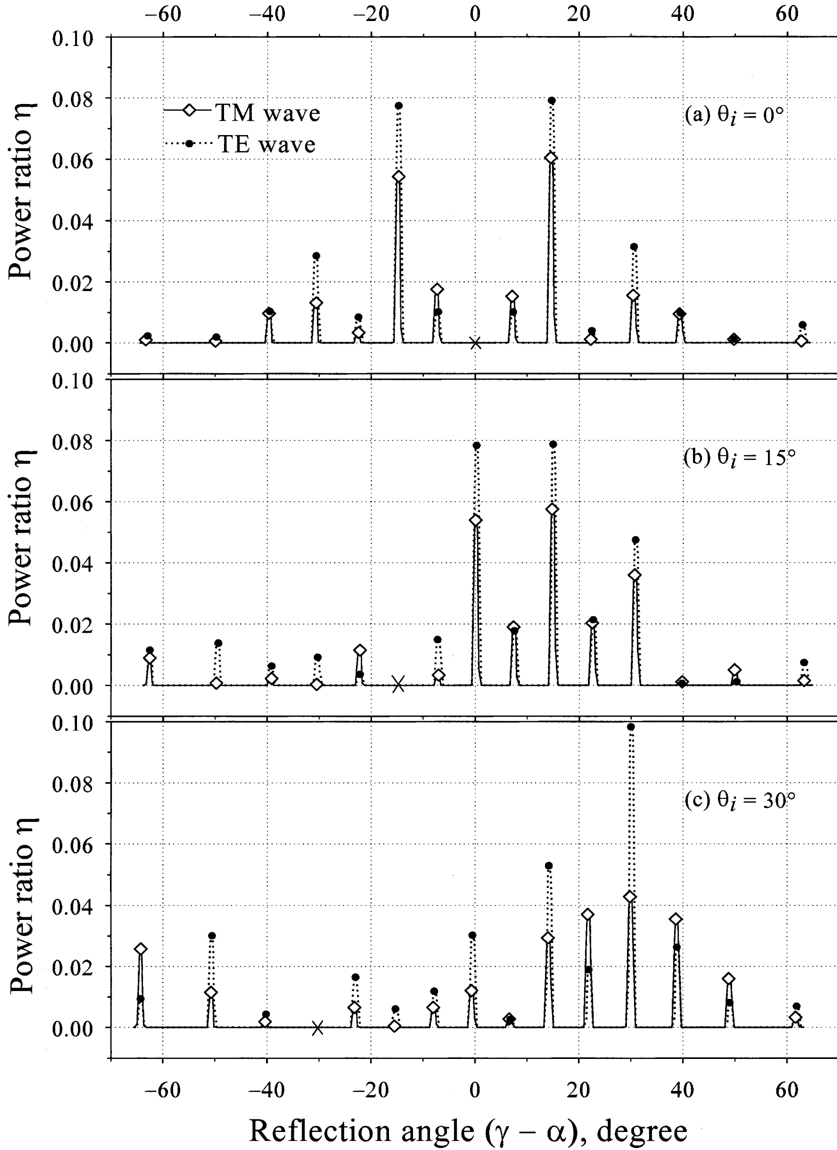

Fig. 4. Bidirectional reflection results of a 1-D grating with $P = 5\,\mu$m and $G = 4\,\mu$m. The "×" sign indicates the angle for which reflection cannot be measured. The incidence angles are (a) $\theta_i = \alpha = 0°$, (b) $\theta_i = \alpha = 15°$, and (c) $\theta_i = \alpha = 30°$.

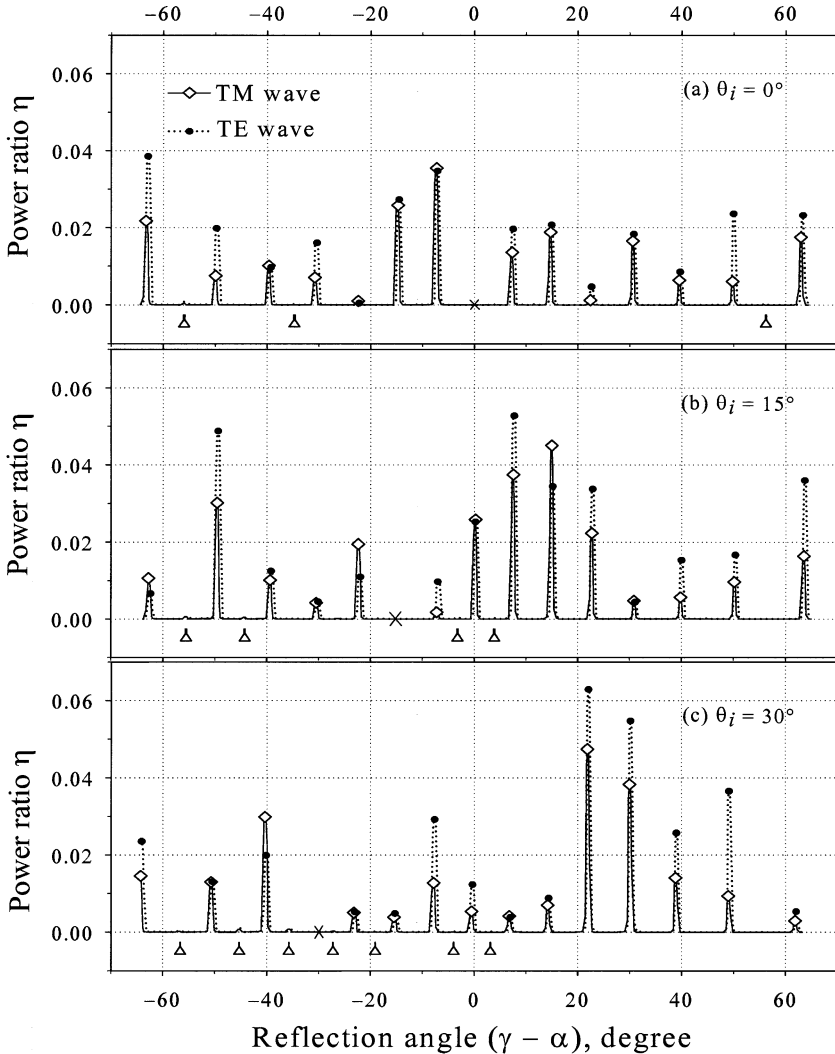

Fig. 5. Bidirectional reflection results of a 1-D grating with $P = 5\,\mu$m and $G = 1\,\mu$m. Triangular indicators point to the locations where the diffraction of a period of $10\,\mu$m were observed. The "×" sign indicates the angle for which reflection cannot be measured. The incidence angles are (a) $\theta_i = \alpha = 0°$, (b) $\theta_i = \alpha = 15°$, and (c) $\theta_i = \alpha = 30°$.

As shown in Fig. 5b and c, the power ratio for the zeroth-order diffraction is not the highest, except for the TM wave at $\theta_i = 15°$. In fact, η for the TE wave at $\theta_i = 15°$ is smaller at $m = 0$ and 1 than at $m = -8$, -1, and 5. At $\theta_i = 15°$, η is smaller for the TE wave than for the TM wave

in the specular direction. This result is the opposite of the reflection from a smooth surface, where the reflectance is slightly higher for the TE wave than for the TM wave. Half of the diffraction orders for the $10\,\mu$m period will overlap with those for the $5\,\mu$m period. Therefore, the peaks may be contributions from the diffraction of both periods. As a result, structures on the surface strongly affect the directional radiative properties of the sample. Theoretical calculations of the power ratio for different orders are undertaken using electromagnetic wave theory and will be compared with these measurements in the future.

The reflection measurement results for a 2-D microstructured sample ($G_1 = 1\,\mu$m and $G_2 = 4\,\mu$m) are shown in Fig. 6 for $\theta_\mathrm{i} = 0°$ and 30°. The actual 2-D microstructures, as shown in Fig. 2c, do not have the exact G_1 and G_2 as initial design dimension shown in Fig. 1b due to the fabrication process. But their periods are the same ($P_1 = P_2 = 5\,\mu$m). The measurements were performed at $\varphi_\mathrm{i} = 0$, 45, and 90° by rotating the sample to observe the diffraction patterns in the different directions. The detector is always in the horizontal plane ($\beta = 0°$) for the measurements. In general, the power ratio at the diffraction peaks for 2-D microstructured samples is much smaller than that for 1-D microstructured samples. The power ratio in Fig. 6 is plotted on a logarithmic scale, and only the peak power ratios are shown. For $\varphi_\mathrm{i} = 0°$, the groove width corresponds to $G_1 = 1\,\mu$m, and it is clear that the diffraction pattern is associated with a period of $10\,\mu$m. The power ratio is generally larger for $\varphi_\mathrm{i} = 90°$ than for $\varphi_\mathrm{i} = 0°$. Hence, higher orders of diffraction were observed for $\varphi_\mathrm{i} = 90°$. The locations of the diffraction peaks for $\varphi_\mathrm{i} = 45°$ can be predicted from Eq. (2) by using the period $\Lambda = P/\sqrt{2}$. This is because the same period, and the diffraction of $\varphi_\mathrm{i} = 45°$, is caused by the periodic structure along the diagonal of the sample. At normal incidence, the power ratio is somewhat symmetric with respect to the specular direction, where $\theta_\mathrm{i} = 30°$, and η is the largest in the specular direction. For $\varphi_\mathrm{i} = 90°$, the power ratios at $m = \pm 1$ are larger than those at $m = \pm 2$, contrary to the behavior of the 1-D structured sample shown in Fig. 4.

The theoretical diffraction positions of the 2-D microstructured sample are essentially Fourier transforms of the patterned structures, and can be predicted using the Fraunhofer diffraction theory [26]. One can also use the simple 1-D grating formula given in Eq. (2) to determine the angular positions of the diffraction. If the structures on the sample have a period along a certain direction, the diffraction will be distributed along that direction, which is determined by φ_r. For example, since the 2-D samples have a period along the $y = x$ direction, there is diffraction along $\varphi_\mathrm{r} = 45°$. If the periods of the structures are the same in both the x and y directions, as in the cases studied here, $P_1 = P_2 = P$. In the direction

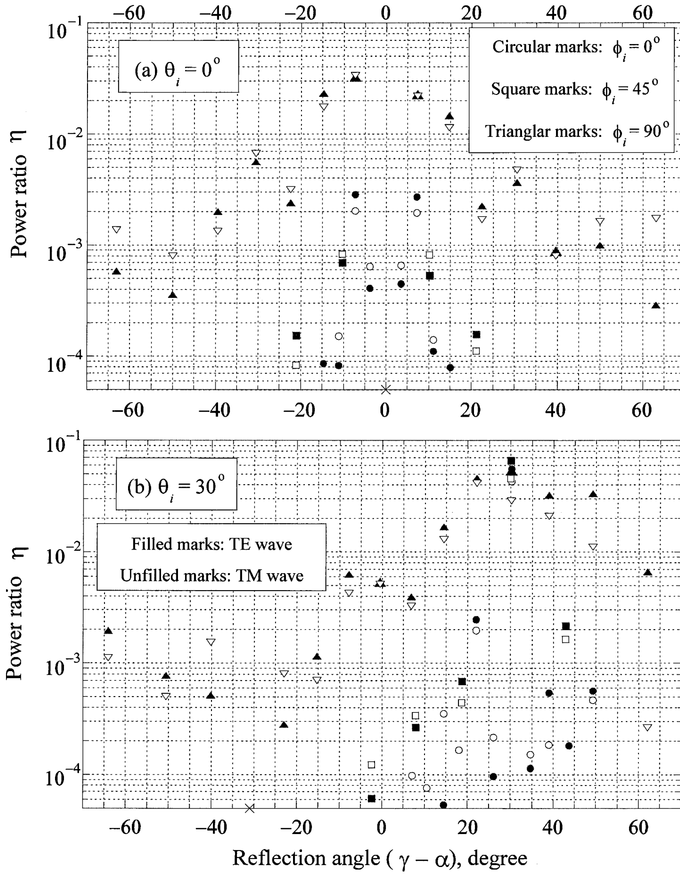

Fig. 6. Power ratio versus diffraction order for a 2-D microstructured sample ($G_1 = 1\,\mu$m, $G_2 = 4\,\mu$m) with different orientations $\varphi_{\mathrm{i}} = 0°$ (circles), 45° (squares), and 90° (triangles). The "×" sign indicates the angle for which reflection cannot be measured. Filled marks are for the TE wave and unfilled marks are for the TM wave. The incidence angles are (a) $\theta_{\mathrm{i}} = \alpha = 0°$ and (b) $\theta_{\mathrm{i}} = \alpha = 30°$.

determined by m structures along the x-axis and n structures along the y-axis, $\varphi_{\mathrm{r}} = \tan^{-1}(n/m)$. The polar angles of diffraction at normal incidence ($\theta_i = \alpha = 0$) can be calculated by

$$\theta_{\mathrm{d}}^{(m,n)} = \sin^{-1}\left(\frac{\lambda\sqrt{m^2+n^2}}{P}\right). \qquad (3)$$

The integer pair (m, n) may be considered as the 2-D diffraction order.

Figure 7 shows the observed diffraction pattern for a 2-D microstructured sample which has features with $G_1 = G_2 = 4\,\mu$m at normal incidence. Here, ψ_x is the angle between the reflection direction projected to the $x-z$ plane and the z-axis, and ψ_y is the angle between the reflection direction projected to the $y-z$ plane and the z-axis. Hence,

$$\begin{aligned} \tan \psi_x &= \tan \theta_r \cos \varphi_r \\ \tan \psi_y &= \tan \theta_r \sin \varphi_r. \end{aligned} \tag{4}$$

Note that $\psi_x = \gamma$ but ψ_y is different from β; see Eq. (1). It can be seen that the diffraction pattern is symmetric with respect to $\psi_x = 0°$ and nearly symmetric along the diagonal. The predicted angular locations of the diffraction orders and the experimental results are listed in Table I for $\gamma \geqslant 0$, along with the measured power ratios. It can be seen that the power ratio is similar for both the TE and TM waves. The agreement between the predicted and measured angular positions of the diffraction orders is within the uncertainty of the experiments ($\pm 0.2°$), except for (m, n) =

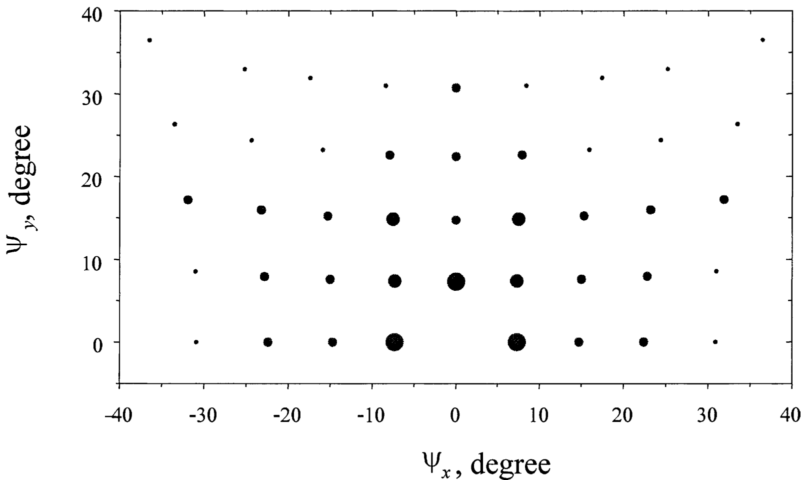

Fig. 7. Diffraction pattern for a 2-D microstructured sample ($G_1 = G_2 = 4\,\mu$m) at normal incidence ($\theta_i = 0°$). The differently sized circles indicate different ranges of the power ratio, averaged over the two polarizations.

Table I. Bidirectional Reflection Results of a 2-D Microstructured Sample (G_1 = 4 μm and G_2 = 4 μm) at Normal Incidence ($\theta_i = 0°$). (Data shown are for $\gamma \geqslant 0$)

	Theoretical values		Experimental values				Power ratio η		
(m, n)	$\varphi_r(°)$	$\theta_r(°)$	$\varphi_r(°)$	$\theta_r(°)$	$\psi_x(°)$	$\psi_y(°)$	TE wave	TM wave	Average
(0, 0)	0	0	--	--	--	--	–	–	–
(1, 0)	0	7.3	0	7.3	7.3	0	1.17×10^{-2}	1.17×10^{-2}	1.17×10^{-2}
(2, 0)	0	14.7	0	14.7	14.7	0	1.51×10^{-3}	1.61×10^{-3}	1.56×10^{-3}
(3, 0)	0	22.4	0	22.4	22.4	0	1.52×10^{-3}	1.48×10^{-3}	1.50×10^{-3}
(4, 0)	0	30.6	0	30.9	30.9	0	4.78×10^{-4}	4.85×10^{-4}	4.82×10^{-4}
(0, 1)	90	7.3	90	7.3	0	7.3	2.12×10^{-2}	1.91×10^{-2}	2.02×10^{-2}
(1, 1)	45	10.4	45.2	10.3	7.3	7.4	3.80×10^{-3}	3.57×10^{-3}	3.69×10^{-3}
(2, 1)	26.6	16.5	26.3	16.7	15.0	7.6	1.42×10^{-3}	1.66×10^{-3}	1.54×10^{-3}
(3, 1)	18.4	23.7	18.3	23.9	22.8	7.9	1.02×10^{-3}	1.05×10^{-3}	1.04×10^{-3}
(4, 1)	14.0	31.6	14.0	31.8	31.0	8.5	4.45×10^{-4}	5.70×10^{-4}	5.08×10^{-4}
(0, 2)	90	14.7	90	14.7	0	14.7	7.91×10^{-4}	1.24×10^{-3}	1.02×10^{-3}
(1, 2)	63.4	16.5	63.6	16.5	7.5	14.8	2.67×10^{-3}	2.72×10^{-3}	2.70×10^{-3}
(2, 2)	45	21.1	44.8	21.1	15.3	15.2	9.05×10^{-4}	1.14×10^{-3}	1.02×10^{-3}
(3, 2)	33.7	27.3	33.7	27.3	23.2	15.9	9.76×10^{-4}	1.02×10^{-3}	9.98×10^{-4}
(4, 2)	26.6	34.6	26.4	34.8	31.9	17.2	7.47×10^{-4}	8.01×10^{-4}	7.74×10^{-4}
(0, 3)	90	22.4	90	22.4	0	22.4	5.48×10^{-4}	9.03×10^{-4}	7.20×10^{-4}
(1, 3)	71.6	23.7	71.6	23.7	7.9	22.6	1.08×10^{-3}	1.33×10^{-3}	1.21×10^{-3}
(2, 3)	56.3	27.3	56.4	27.2	15.9	23.2	6.77×10^{-4}	7.03×10^{-4}	6.90×10^{-4}
(3, 3)	45	32.6	44.9	32.7	24.4	24.4	2.84×10^{-4}	3.40×10^{-4}	3.12×10^{-4}
(4, 3)	36.9	39.4	36.8	39.6	33.5	26.3	6.73×10^{-4}	5.73×10^{-4}	6.23×10^{-4}
(0, 4)	90	30.6	90	30.7	0	30.7	1.07×10^{-3}	6.91×10^{-4}	8.81×10^{-4}
(1, 4)	76.0	31.6	76.2	31.7	8.4	31.0	6.10×10^{-4}	6.19×10^{-4}	6.15×10^{-4}
(2, 4)	63.4	34.6	63.3	34.9	17.4	32.0	4.65×10^{-4}	4.17×10^{-4}	4.41×10^{-4}
(3, 4)	53.1	39.4	54.0	38.7	25.2	33.0	1.24×10^{-5}	1.47×10^{-5}	1.36×10^{-5}
(4, 4)	45	45.9	45.0	46.3	36.5	36.4	1.73×10^{-4}	1.79×10^{-4}	1.76×10^{-4}

(4, 0), (2, 4), (3, 4), and (4, 4). When the diffraction spots on the surface of a unit sphere are projected to the vertical $x - y$ plane, shown in Fig. 3b, the distance between adjacent diffraction orders are exactly the same along either axis. This distance is given by λ/P. Although this uniform pattern can also be achieved using imaging optics [26], the present study uses accurate radiometric measurements to obtain quantitative information regarding the directional distribution of the reflected power from the microstructured surface.

5. CONCLUDING REMARKS

2-D microstructured samples have been fabricated using photomask rotation with a 1-D patterned photomask, allowing a high density of periodic structures (2.25×10^6 in $7.5 \times 7.5\,\text{mm}^2$) to be produced. The bidirectional reflection of the 1-D and 2-D microstructured samples, made of lightly doped silicon, has been characterized with high angular resolution. The experimental results presented here, especially those of 2-D microstructured samples, may serve as a benchmark for future theoretical studies. The reflected power ratio depends strongly on the details of the microstructures. The results suggest that it is possible to characterize the microstructures with bidirectional reflection measurements. The periods of the 1-D and 2-D microstructured samples can be determined from the diffraction angles. The shape symmetry of the microstructures may be easily identified by observing the symmetry of the reflected power ratio distribution at normal incidence. Further studies are underway to quantitatively model the power ratio and correlate it with the microstructures of the sample.

ACKNOWLEDGMENTS

This work was supported by the Georgia Tech Focused Research Program and the National Science Foundation (CTS-0236831). Z.M.Z. thanks Professor Levent Degertekin for a valuable discussion.

REFERENCES

1. A. K. Sharma, S. H. Zaidi, P. C. Logofatu, and S. R. J. Brueck, *IEEE J. Quantum Electron.* **38**:1651 (2002).
2. G. Sarusi, B. F. Levine, S. J. Pearton, K. M. S. Bandara, and R. E. Leibenguth, *Appl. Phys. Lett*. **64**:960 (1994).
3. A. Boueke, R. Kuhn, P. Fath, G. Willeke, and E. Bucher, *Solar Energy Mater. Solar Cells* **65**:549 (2001).
4. T. J. Coutts, *Renewable and Sustainable Energy Rev.* **3**:77 (1999).
5. A. Heinzel, V. Boerner, A. Gombert, B. Bläsi, V. Wittwer, and J. Luther, *J. Mod. Opt.* **47**:2399 (2000).
6. Y. Kanamori, K. Hane, H. Sai, and H. Yugami, *Appl. Phys. Lett.* **78**:142 (2001).
7. J. P. Hebb, K. F. Jensen, and J. Thomas, *IEEE Trans. Semocond. Manuf.* **11**:607 (1998).
8. Z. M. Zhang, *Annu. Rev. Heat Transfer* **11**:351 (2000).
9. S. S. H. Naqvi, R. H. Krukar, J. R. McNeil, J. E. Franke, T. M. Niemczyk, D. M. Haaland, R. A. Gottscho, and A. Kornblit, *J. Opt. Soc. Am. A* **11**:2485 (1994).
10. J. Homola, I. Koudela, and S. S. Yee, *Sens. Actuators B* **54**:16 (1999).
11. D. K. Kambhampati, T. A. M. Jakob, J. W. Robertson, M. Cai, J. E. Pemberton, and W. Knoll, *Langmuir* **17**:1169 (2001).
12. R. B. Zipin, *Appl. Opt.* **5**:1954 (1966).

13. Z. M. Zhang, C. J. Fu, and Q. Z. Zhu, *Adv. Heat Transfer* **37**:179 (2003).
14. P. J. Hesketh, J. N. Zemel, and B. Gebhart, *Nature* **324**:549 (1986).
15. P. J. Hesketh, B. Gebhart, and J. N. Zemel, *J. Heat Transfer* **110**:680 (1988).
16. T. K. Wang and J. N. Zemel, *Appl. Opt.* **32**:2021 (1993).
17. J.-J. Greffet, R. Carminati, K. Joulain, J. P. Mulet, S. Mainguy, and Y. Chen, *Nature* **416**:61 (2002).
18. R. Carminati and J.-J. Greffet, *Phys. Rev. Lett.* **82**:1660 (1999).
19. H. Sai, H. Yugami, Y. Akiyama, Y. Kanamori, and K. Hane, *J. Opt. Soc. Am. A* **18**:1471 (2001).
20. S. Maruyama, T. Kashiwa, H. Yugami, and M. Esashi, *Appl. Phys. Lett.* **79**:1393 (2001).
21. D. W. Cohn, K. Tang, and R. O. Buckius, *Int. J. Heat Mass Transfer* **40**:3223 (1997).
22. K. Tang and R. O. Buckius, *Microscale Thermophys. Eng.* **2**:245 (1998).
23. Y. J. Shen, Q. Z. Zhu, and Z. M. Zhang, *Rev. Sci. Instrum.* **74**:4885 (2003).
24. M. J. Madou, in *Fundamentals of Microfabrication* (CRC Press, Boca Raton, Florida, 2002), Chap. 2.
25. P. Beckmann and A. Spizzichino, *The Scattering of Electromagnetic Waves from Rough Surfaces* (Artech House, Norwood, Massachusetts, 1987), Chap. 4.
26. J. W. Goodman, *Introduction to Fourier Optics* (McGraw-Hill, New York, 1968).